# *Foldable Joints for Foldable Robots*

# Foldable Joints for Foldable Robots

**Cynthia Sung**
Computer Science and
Artificial Intelligence Laboratory,
Massachusetts Institute of Technology,
Cambridge, MA 02139
e-mail: crsung@csail.mit.edu

**Daniela Rus**
Computer Science and
Artificial Intelligence Laboratory,
Massachusetts Institute of Technology,
Cambridge, MA 02139
e-mail: rus@csail.mit.edu

*Print-and-fold manufacturing has the potential to democratize access to robots with robots that are easier to fabricate using materials that are easier to procure. Unfortunately, a lack of understanding about how motion can be achieved by folding hinders the scope of print-and-fold robots. In this paper, we show how the basic joints used in robots can be constructed using print-and-fold. Our patterns are parameterized so that users not only get the desired degrees of freedom but can also specify the joint's range of motion. The joints can be combined with each other to achieve higher degrees of freedom or with rigid bodies to produce foldable linkages. We have folded our basic joints and measured their force–displacement curves. We have composed them into joints with higher degrees of freedom and into foldable mechanisms and found that they achieve the expected kinematics. We have also added actuators and control circuitry to our joints and mechanisms, showing that it is possible to print and fold entire robots with many different kinematics using a uniform process.* [DOI: 10.1115/1.4029490]

*Keywords: foldable joints, linkages, origami-inspired design, print-and-fold robots*

## 1 Introduction

Rapid fabrication of robots is a long-held goal for many engineers. Recent work combining planar fabrication techniques with origami-inspired designs has shown that functional robots can be created within a day [1,2]. This print-and-fold paradigm of manufacturing promises lower complexity since one uniform process is used to fabricate every part of the robot, and movable parts such as limbs and joints are constructed no differently from rigid bodies.

Many foldable robot designs have been developed [3–6], but the motions achieved by these designs are simple compared to robots manufactured using standard machining and assembly. In particular, most robot designs rely on movement generated by single independent folds (refer Fig. 1); that is to say, they make use only of hingelike motions.

Progress beyond these structures is complicated by a lack of understanding of what types of motions can result from folding. The majority of theoretical work in design of folded structures (see Ref. [7] for a review) focuses on the creation of rigid bodies and does not extend to transformable structures, or structures that can move. Transformable folded structures were tested in Refs. [8–10] or analyzed in Refs. [11–13], but the resulting fold patterns are application-specific and do not translate well to general robot design. In Ref. [14], the authors analyzed and categorized pop-up mechanisms, and they used their findings to propose new pop-up joint types. A similar classification scheme for action origami was proposed in Ref. [15], but although many models from popular literature were classified, no conclusions were drawn on how to use the classification to generate new action origami models.

In mechanism design not restricted to folding, the joints and links that are used to produce motion are readily available and can straightforwardly be connected together, making methods for automated mechanism design [16–19] and analysis [20] possible. Our approach is to enable such mechanism design tools to be used with folded structures by providing the necessary vocabulary of foldable joints. In this paper,[1] we contribute fold patterns for revolute and prismatic joints that:

- are parameterized to achieve a user-specified size and range of motion
- can be composed with each other into joints with higher degrees of freedom
- can be composed with rigid bodies to produce foldable linkage mechanisms
- provide natural placement of actuators, and
- have been incorporated into designs for foldable robots that have been experimentally validated.

We have also folded our joints and compared their force–displacement curves to a pseudo-rigid-body model [23]. Our designs open the way to making robots with any desired kinematics from a single sheet using print-and-fold.

## 2 Parameterized Joint Patterns

Our mechanisms and robots are based on three joint types, a hinge joint, a prismatic joint, and a pivot joint. In this section, we present the parameterized fold patterns for each.

**2.1 Definitions.** We begin with informal definitions for the terms used in the following descriptions. A more formal treatment of folding theory can be found in Ref. [7]. Consider a nonself-intersecting 2D polygon $P$ (possibly with holes). A *fold* on $P$ is a line segment such that both endpoints are on the boundary of $P$ and the segment itself lies on the interior of $P$. A *fold pattern* consists of such a polygon $P$ and a set of folds on $P$. Each fold is associated with a fold angle in the range $(-\pi, \pi)$. When all fold angles are single values, then a fold pattern produces a static structure. Since in this paper, we are interested in patterns for joints, which allow movement, some folds must be able to achieve entire fold angle ranges, which are connected subsets of $(-\pi, \pi)$. We call these folds the *active* folds. In this paper, figures depicting fold patterns will show cut lines forming the boundary of $P$ in solid black, active folds in solid gray, and all other folds in dotted gray.

The folds in a fold pattern divide the original polygon $P$ into *faces*, smaller polygons that overlap only at the fold lines. Since the purpose of joints is to connect other structures to each other, our joints have faces that exist specifically to attach to other bodies. We call these faces the *bases* of the joint. All of our joints are designed to connect two structures to each other and so each has two bases.

[1]Parts of this work were previously published in Ref. [21].

Manuscript received August 2, 2014; final manuscript received December 23, 2014; published online February 27, 2015. Assoc. Editor: Aaron M. Dollar.

  

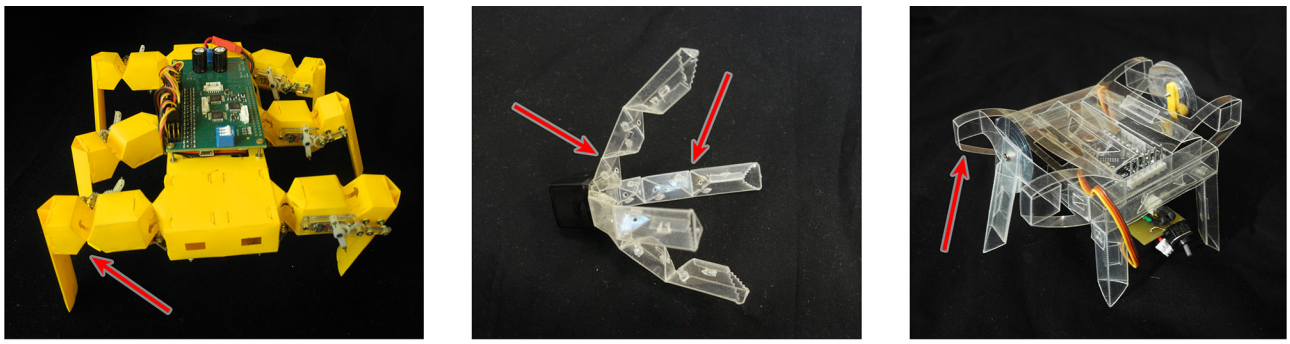


**Fig. 1 Previous foldable robots, joints indicated by arrows. They all use single-fold joints. (*a*) Hexapod [3], (*b*) gripper [4], and (*c*) hexapod [6].**

**2.2 Hinge Joint.** Hinge joints enable rotation about an axis parallel to a base and can be implemented as a single active fold on the base itself. This is the approach taken in previously designed foldable robots (refer Fig. 1). However, when hinge joints are created in this way, the joint itself consists of a single fold and occupies zero volume. As a result, the joint limits depend on the geometry of the bodies being connected and cannot be independently specified.

*Joint Description.* We have designed a hinge joint of a more general form, shown in Fig. 2(*a*). The base of the joint is a regular polygon with $N_s$ sides ($N_s = 6$ in the example), where $N_s$ is even. From two opposite sides, sloped faces angle to meet at the axis of rotation. Triangular faces are attached to all other sides of the bases to provide structural support.

When the joint moves, the top base rotates about the axis of rotation relative to the bottom base. The limits of the rotational motion are when two rectangular faces touch. Thus, the angle between a rectangular face and the base it is connected to is determined by the joint limits as $R/4$, where $R$ is the total desired angular range of motion.

*Fold Pattern.* The associated fold pattern is a strip that attaches to the outer edges of the base polygons and contains the rectangular and triangular faces. Additional folds that tuck away extra material help form the hinge shape. Input parameters to the pattern are the number of sides $N_s$, the radius $r$ of the base, and the total range of motion $R$. The hinge joint is always symmetric. If asymmetric joint limits are desired, users can attach the joint at an angle by attaching a sloped polyhedron to the base first, as we do for the mechanism in Fig. 22. Note that the joint angle is restricted to be between $-\pi$ and $\pi$ radians, and that the length of the joint increases with the range of motion.

### 2.3 Prismatic Joint

*Joint Description.* A prismatic joint is created by composing parallelogram linkages to produce linear motion of a desired distance without increasing the size of the joint. Each base of the joint is a rectangular face that forms one side of a parallelogram linkage. In a single parallelogram linkage, horizontal and vertical translations are coupled. By connecting linkages in a grid, these two degrees of freedom can be decoupled. Figure 2(*b*) shows a two-by-two grid of linkages of height $h$. By restricting horizontal motion, the joint enables vertical translation by as much as $2h$. By restricting the vertical distance between the bases to be $h$, the joint enables horizontal translation by a distance $h\sqrt{3}$ in either direction.

The resulting structure enables two degree-of-freedom motion in a plane. To produce a true prismatic joint, which allows linear motion in one direction but not in any other, we impose a height constraint to the joint using additional faces added in a subsequent stage (refer mechanism in Fig. 22). This yields a joint with translational motion parallel to the base.

*Fold Pattern.* The fold pattern for the grid of parallelogram linkages is a grid of rectangular faces, built by repeating and connecting units as shown in Fig. 3. On the leftmost side is a unit consisting of four faces that fold into a parallelogram linkage. To add columns, three-face add-on units are attached to the right, with the fold angles of each unit opposite in sign to the one before. For each layer, the entire row of units is duplicated and attached above the previous layer to the faces corresponding to the top link of the

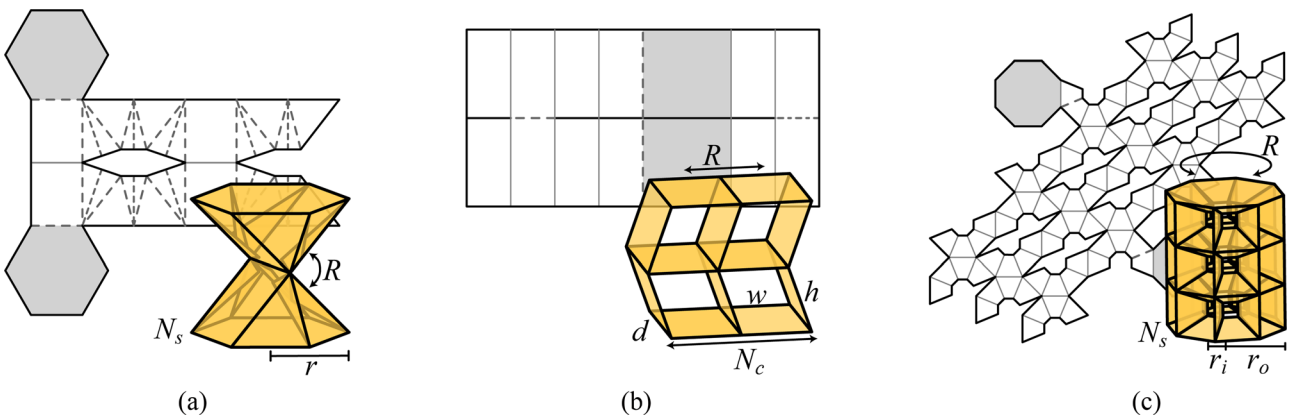


**Fig. 2 Summary of fold patterns and folded states for three basic joint types with input parameters indicated. The base faces are shaded. (*a*) Hinge joint, (*b*) prismatic joint, and (*c*) pivot joint.**

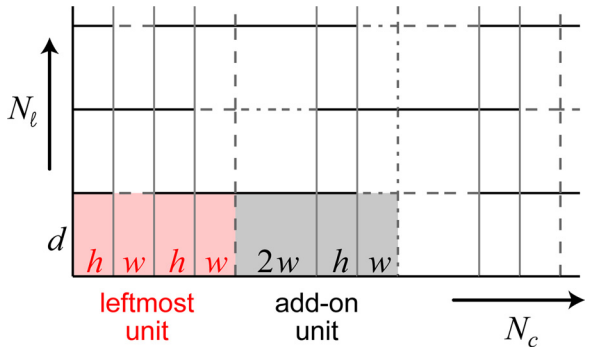


**Fig. 3 Prismatic joint construction**

linkage below. Input parameters are the dimensions $h$, $w$, and $d$ of one linkage in the grid, the joint's horizontal range of motion $R$, and the number of columns $N_c$ in the grid. Assuming that the height of the linkage is constrained to be $h$, the theoretical number of layers $N_\ell$ can be computed using the relationship $R = 2h\sqrt{N_\ell^2 - 1}$, although practically we compute $N_\ell$ using the simpler expression $R = 2h(N_\ell - 1)$. The joint's range of motion can be increased by changing either $h$ or $N_\ell$.

### 2.4 Pivot Joint

*Joint Description.* Pivot joints allow rotation about an axis perpendicular to the base. To achieve this twisting motion, we use parallelogram linkages arranged in a cycle. Figure 4 shows an example of five folded square linkages in this configuration. The black outlines indicate the corresponding 3D linkage, and the gray lines indicate folds, which correspond to the axes of rotation for the joints of the black linkage. When this arrangement of faces is used, a twist-and-collapse motion results. Note that this motion is theoretically not rigid, since it requires elongation of some of the edges. It is possible to create a rigidly foldable structure by adding triangular pleats to the corners of each of the square linkage to allow stretch. Since our simulations show that the amount of elongation is at most 1% (refer Fig. 5), and foldable robots have generally been fabricated from flexible materials, we use the simpler design shown and accommodate some stretch by replacing one fold out of the four in each square linkage with a cut.

The bases of the pivot joint are regular polygons, and each side is attached to one square linkage. In the same way as for the prismatic joint, we stack linkages in series to decouple vertical translation from twisting motion. Figure 2(*c*) shows an eight-sided three-layer stacked linkage structure. When the relative rotation of the two bases is maintained at 0, the linkage can achieve a vertical translation of up to $6r_o \sin(\pi/8)$. Restricting the distance between the two bases to be the height of one layer using additional faces enables pure twisting motion. We add faces for height constraints in subsequent steps.

*Fold Pattern.* The pattern is built similarly to the prismatic joint, by repeating and connecting identical units. The unit, shown in Fig. 6, consists of four isosceles trapezoids, each with an angle

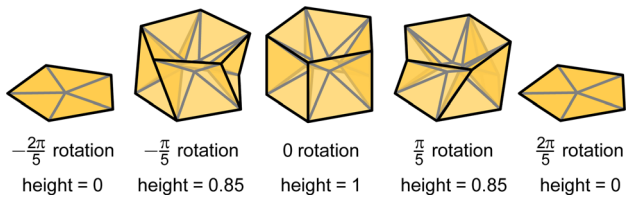


**Fig. 4 Motion of one layer of a pivot joint. Black lines have length 1.**

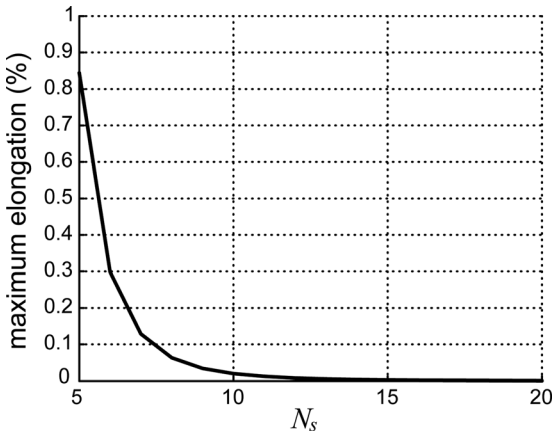


**Fig. 5 Maximum elongation of folds in a pivot joint over the course of rotation**

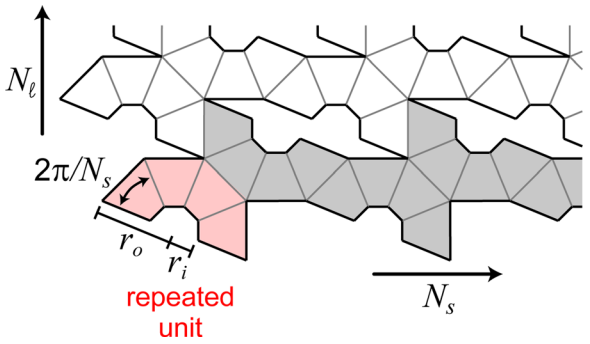


**Fig. 6 Pivot joint construction**

equal to $2\pi/N_s$ between the legs of the trapezoid, connected along the legs. $N_s$ units are attached to each other at the faces corresponding to the side links of the linkages in order to produce the $N_s$ linkages that form one layer of the joint (shaded gray). The resulting strip of units is duplicated once for each layer and attached to the adjacent layers using the faces corresponding to the top and bottom links of the linkages. Input parameters to this design are the number of sides $N_s > 4$ of the base, the range of motion $R$, and the inner and outer radii $r_i$ and $r_o$ of the joint. Similarly to the prismatic joint, we approximate the number of layers $N_\ell$ using the expression $R = (4\pi/N_s)(N_\ell - 1)$. In Fig. 2(*c*), the joint has eight sides and three layers and can twist $\pi$ radians.

## 3 Pseudo-Rigid-Body Model

Folded structures are compliant mechanisms whose faces and folds all deform with external forces. However, such compliant mechanisms can be modeled as mechanisms where rigid bodies are joined at hinges with torsion springs [22,23], a method that was applied to folded cartons in Refs. [24] and [25]. In this section, we present a model for our folded joints, which we later compare to experimental measurements.

**3.1 Hinge Joint.** A hinge joint is two rigid bodies connected at two active folds. Figure 7 shows a cross-sectional view of the hinge joint. The angle $\theta$ is the joint angle and folds 1 and 2 are the active folds. Let $\phi_1$ and $\phi_2$ represent the fold angles of the folds 1 and 2, respectively. These fold angles are functions of the joint angle

$$\phi_1 = R/2 + \theta \tag{1}$$

$$\phi_2 = R/2 - \theta \tag{2}$$

where $R$ is the range of motion of the joint.

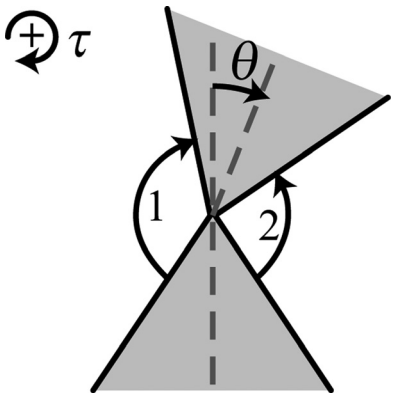


**Fig. 7 Cross-sectional view of hinge joint with active folds labeled**

Then the holding torque $\tau$ necessary to maintain the joint at a specific angle is

$$\tau(\theta) = -k_1(\phi_1 - \phi_1^o) + k_2(\phi_2 - \phi_2^o) \tag{3}$$

where stiffnesses $k_1$ and $k_2$ may be functions of $\theta$ and $\phi_1^o$ and $\phi_2^o$ are the equilibrium positions of the active folds. When the stiffnesses $k_1 = k_2 = k$ and using Eqs. (1) and (2), this expression simplifies to

$$\tau(\theta) = -2k\left(\theta - \frac{\phi_1^o - \phi_2^o}{2}\right) \tag{4}$$

That is to say, the joint as a whole acts as a torsion spring with spring constant equal to the sum of the spring constants of the active folds.

Since each of our joints is constructed from a single sheet of material, the stiffness $k$ as a function of $\theta$ can be computed as [23]

$$k = K_\Theta \frac{EI}{\ell} \tag{5}$$

where $K_\Theta$ is the nondimensionalized stiffness, $E$ is the Young's modulus of the material, $I$ is the area moment of inertia of the section of material involved in the fold, and $\ell$ is the length of the pivot. Since the folds are perforated using the laser cutter, it is difficult to calculate the moment of inertia $I$ for a fold exactly. However, we expect a constant proportion of the material is removed during perforation, so

$$I \propto \ell_f t^3 \tag{6}$$

where $\ell_f$ is the length of the fold and $t$ is the thickness of the material. That is, for a given material, the stiffness $k$ varies with $\ell_f t^3$.

**3.2 Prismatic Joints.** Prismatic joints are formed by stacking parallelogram units. We first consider a two-layer prismatic joint. To formulate the pseudo-rigid-body model [23], we use the equivalent linkage shown in Fig. 8(*a*), where the fold angles of the active folds are labeled. Since each unit is a parallelogram, all folds labeled 1 must have the same fold angle. In addition, it is reasonable to assume for the sake of simplicity that all of these folds labeled 1 have the same stiffness and equilibrium position, since they are all fabricated identically and they all experience the same motions. This is similarly true for the folds labeled 1′, 2, and 2′, respectively.

In that case, it is possible to simplify the prismatic joint to the diagram in Fig. 8(*b*), where the folds in the bottom row of units are reduced to a single equivalent active fold that produces a torque

$$\tau_1 = k_1(\phi_1 - \phi_1^o) \tag{7}$$

on link $L_1$, where $\phi_1$ is the angle at fold 1, and the top row of units is reduced to a single active fold that produces a torque

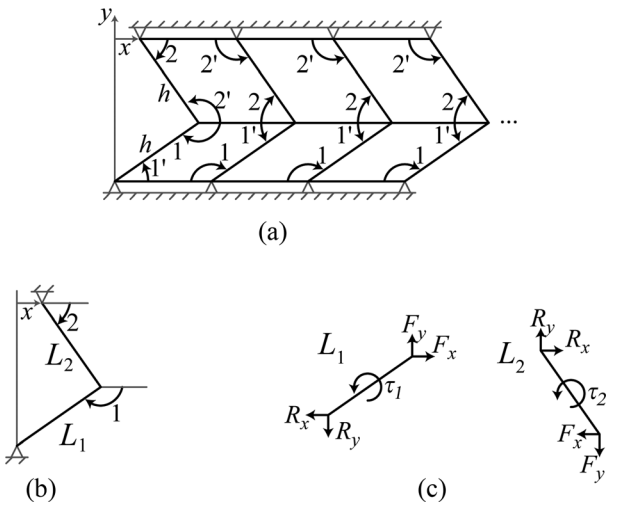


**Fig. 8 (*a*) Diagram of two-layer prismatic joint with active folds labeled. (*b*) Simplified linkage diagram. (*c*) Free-body diagram for individual links in (*b*).**

$$\tau_2 = k_2(\phi_2 - \phi_2^o) \tag{8}$$

on link $L_2$, where $\phi_2$ is the angle at fold 2. The distance $x$ is the joint position. To enable horizontal translation, the total height of the linkage is maintained at $h$, so the following relations must hold:

$$h\cos\phi_1 + h\cos\phi_2 = x \tag{9}$$

$$h\sin\phi_1 + h\sin\phi_2 = h \tag{10}$$

To compute the holding force $R_x$ necessary to maintain the joint at a specific position $x$, we use the following force balance equations. For link $L_1$

$$F_x - R_x = 0 \tag{11}$$

$$F_y - R_y = 0 \tag{12}$$

$$\tau_1 - hR_x\sin\phi_1 - hR_y\cos\phi_1 = 0 \tag{13}$$

Similarly, for link $L_2$

$$\tau_2 - hR_x\sin\phi_2 - hR_y\cos\phi_2 = 0 \tag{14}$$

So the holding force $R_x$ can be found by solving the following matrix equation for $F_x$:

$$h\begin{bmatrix}\sin\phi_1 & \cos\phi_1\\ \sin\phi_2 & \cos\phi_2\end{bmatrix}\begin{bmatrix}R_x\\ R_y\end{bmatrix} = \begin{bmatrix}\tau_1\\ \tau_2\end{bmatrix} \tag{15}$$

It is simple to see that adding more layers to the prismatic joint just adds more rows to the matrix equation and more variables to the distance constraints. Thus, the relationship between holding force and fold torques is

$$h\begin{bmatrix}\sin\phi_1 & \cos\phi_1\\ \sin\phi_2 & \cos\phi_2\\ \sin\phi_3 & \cos\phi_3\\ \cdots & \cdots\end{bmatrix}\begin{bmatrix}R_x\\ R_y\end{bmatrix} = \begin{bmatrix}\tau_1\\ \tau_2\\ \tau_3\\ \cdots\end{bmatrix} \tag{16}$$

subject to

$$\sum_{i=1}^{N_\ell} h\cos\phi_i = x \tag{17}$$

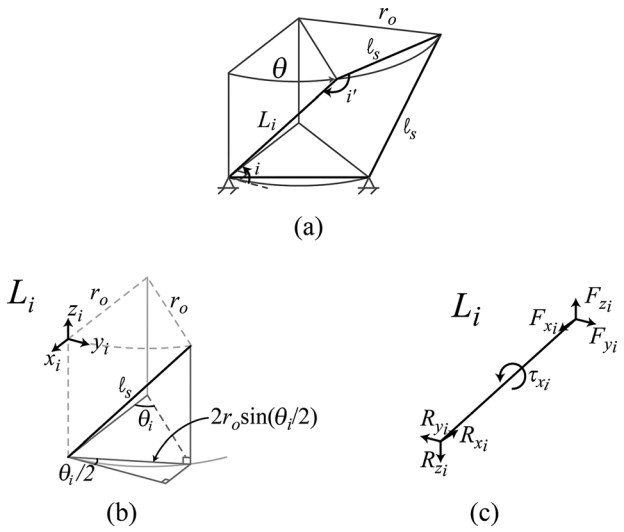


**Fig. 9 (*a*) Diagram of a single square linkage on a pivot joint. (*b*) Link $L_i$. (*c*) Free-body diagram of link $L_i$.**

$$\sum_{i=1}^{N_\ell} h\sin\phi_i = h \tag{18}$$

**3.3 Pivot Joint.** Since the pivot joint consists of layers of parallelogram units similarly to the prismatic joint, we expect it to follow a similar model. In particular, Fig. 9(*a*) shows a single square linkage on a pivot joint. Since the joint is rotationally symmetric, the analysis for every link $L_i$ in a single layer of the joint is the same. Let $\phi_i$ be the measure of fold angle $i$ as indicated in the figure, and let $\theta_i(\phi_i)$ denote the rotation about the center axis of the pivot joint that is contributed by layer $i$. The length $\ell_s = 2r_o\sin(\pi/N_s)$ is the length of one side of the pivot joint, and also the length of each link on the corresponding linkage.

To construct a pseudo-rigid-body model, we approximate the torque on the link $L_i$ contributed by the fold at $i$ as

$$\tau_i = k_i(\phi_i - \phi_i^o) \tag{19}$$

and assume all links rigid [23]. The height of layer $i$ is $\sqrt{\ell_s^2 - (2r_o\sin(\theta_i(\phi_i)/2))^2} = 2r_o\sqrt{\sin^2(\pi/N) - \sin^2(\theta_i(\phi_i)/2)}$. When the joint is constrained to a total height of $\ell_s$, the following geometrical relations must hold:

$$\sum_{i=1}^{N_\ell}\theta_i(\phi_i) = \theta \tag{20}$$

$$2r_o\sum_{i=1}^{N_\ell}\sqrt{\sin^2\frac{\pi}{N} - \sin^2\frac{\theta_i(\phi_i)}{2}} = \ell_s \tag{21}$$

To calculate the holding torque, we use the free-body diagram of link $L_i$ shown in Fig. 9(*c*). The joint produces rotational motion. For a single link, we align the $x_i$ direction radially outward from the center of the joint, according to the bottom attachment point, the $z_i$ direction parallel to the center axis of the joint, and the $y_i$ direction according to the right-hand convention. Then the force balance equations are as follows:

$$F_{x_i} - R_{x_i} = 0 \tag{22}$$

$$F_{y_i} - R_{y_i} = 0 \tag{23}$$

$$F_{z_i} - R_{z_i} = 0 \tag{24}$$

$$\tau_{x_i} - 2r_oR_{y_i}\sqrt{\sin^2\frac{\pi}{N} - \sin^2\frac{\theta_i(\phi_i)}{2}} - r_oR_{z_i}\sin\theta_i(\phi_i) = 0 \tag{25}$$

The total holding torque for that layer is equal to $\tau_{\theta_i} = N_sr_oR_{y_i}$.

Between adjacent layers, the holding torque for those two layers must be equal at equilibrium

$$\tau_{\theta_i} = \tau_{\theta_{i-1}} \tag{26}$$

which implies $R_{y_i} = R_{y_{i-1}} = R_y$. We can therefore compute the reaction forces by solving the following matrix equation:

$$r_o\begin{bmatrix} 2\sqrt{\sin^2\frac{\pi}{N} - \sin^2\frac{\theta_1(\phi_1)}{2}} & \sin\theta_1(\phi_1) \\ 2\sqrt{\sin^2\frac{\pi}{N} - \sin^2\frac{\theta_2(\phi_2)}{2}} & \sin\theta_2(\phi_2) \\ 2\sqrt{\sin^2\frac{\pi}{N} - \sin^2\frac{\theta_2(\phi_2)}{2}} & \sin\theta_3(\phi_3) \\ \cdots & \cdots \end{bmatrix}\begin{bmatrix} R_y \\ R_z \end{bmatrix} = \begin{bmatrix} \tau_{x_1} \\ \tau_{x_2} \\ \tau_{x_3} \\ \cdots \end{bmatrix} \tag{27}$$

subjected to constraints Eqs. (20) and (21). The net holding torque for the joint is then equal to $\tau_\theta = N_sr_oR_y$.

## 4 Experimental Results

We have built a system that allows users to specify a type of joint and the desired parameters and that automatically produces the corresponding fold pattern. We generated fold patterns for our basic joints and constructed them out of 0.051 mm and 0.127 mm thick polyester film, cutting them using a laser cutter and perforating the folds for easier assembly. Before printing, we added tabs and slots to the pattern to attach edges that should remain coincident in the folded state.

Figure 10 shows two of our folded joints. Figure 10(*a*) shows the result for a $N_c = 2$, $N_\ell = 4$ prismatic joint folded from 0.127 mm thick film, where every layer has height $h = 15$ mm. Without height constraints, it is capable of 90 mm horizontal motion and 60 mm vertical motion. Figure 10(*b*) shows a six-sided pivot joint with $r_o = 44$ mm and a $2\pi$ radian range of motion, folded from 0.127 mm thick film. The faces corresponding to one square linkage are outlined. The joint has four layers and is constrained in

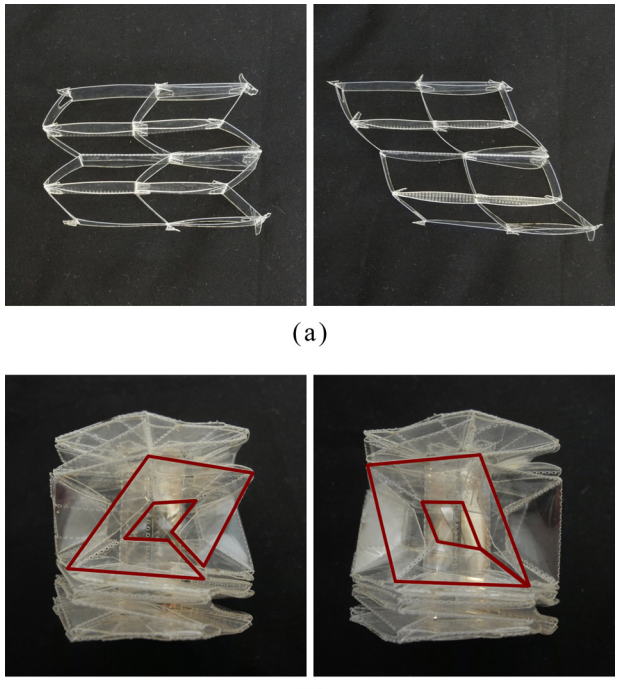


**Fig. 10 Joints folded from polyester film in two different positions. (*a*) Prismatic joint and (*b*) pivot joint.**

height by additional faces subsequently added to the fold pattern. In particular, we added a tube of the desired height down the center of the joint; we attached it to the base on one side of the joint and to an added perpendicular face on the other side (refer Fig. 20 for fold pattern). In this way, the bases can rotate relative to each other but cannot move farther apart than the length of the tube. Since plastic film has thickness, adding layers to increase a joint's range of motion increases the size of the joint: Each layer adds the thickness of five sheets of plastic in the case of the prismatic joint, and four sheets of plastic for the pivot joint. For the joint in Fig. 10(*b*), the additional thickness corresponds to almost half the joint length. This is not a concern for the hinge joint, which does not rely on layers to control the range of motion.

**4.1 Force and Torque Measurements.** To check the spring-based models derived in Sec. 3, we generated and folded designs for multiple hinge, prismatic, and pivot joints and measured the holding forces and torques for a range of positions.

*4.1.1 Hinge Joint.* For the hinge joint, we generated three hinges with four sides ($r = 25$ mm) and varying ranges of motion: $\pi/2$ radians, $\pi$ radians, and $3\pi/2$ radians. We folded each design out of both 0.051 mm and 0.127 mm thick polyester film and measured the holding torque of each joint over its entire range of motion. Figure 11 shows the experimental setup and the three joints tested. A Futek TFF500 torque sensor was attached to one base of the hinge joint and measured the torque as a stepper motor moved the other base. A LABVIEW program was used to control the stepper motor and to record torque measurements at 1 kHz. Each hinge was moved one step (200 steps/rev) every 50 ms, first in a clockwise direction to the positive joint limit, then counterclockwise to the negative joint limit, for a total of four repetitions. For each step of the motor, the torque measurements obtained at that step were averaged.

Figures 12 and 13 show the results. Measurements were consistent across runs. For small angular deflections, folds can be approximated by a linear spring model. However, for larger angular deflections, folds start to exhibit nonlinear behavior. Holding torque levels off as the joint angle increases, similarly to the findings in Ref. [25], and even decreases for the thinner 0.051 mm thick material. For the thicker material (0.127 mm thick), the folds show hysteresis, with the amount of hysteresis increasing with the joint range. In the context of our model, this means that the equilibrium position of the joint changes depending on the motion of the joint.

*4.1.2 Prismatic Joint.* To test our model of the prismatic joint, we generated and folded prismatic joints with $N_c \in \{1, 2, 4\}, N_\ell \in \{2, 4, 6, 8\}$, for a total of 12 joints. Each joint had $h = d = 15$ mm with $N_c w = 60$ mm, and we tested a joint range of $2(N_\ell - 1) \times 15$ mm. We used an Instron 5944 machine to measure the holding force for each of the joints. The height of the joint was maintained at 15 mm using the setup shown in Fig. 14. We moved the joint to the negative joint limit at a rate of 10 mm/min, then to the positive joint limit, for a total of three repetitions.

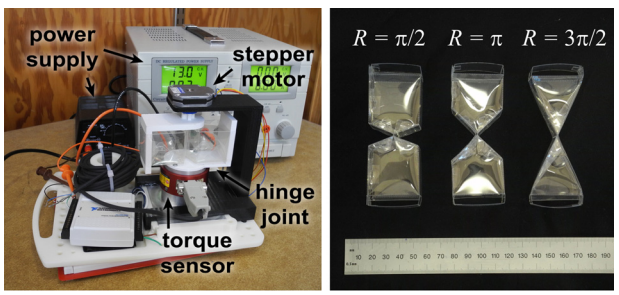


**Fig. 11 Experimental setup used to measure holding torque of the hinge joints. (*a*) Experimental setup and (*b*) tested hinge joints.**

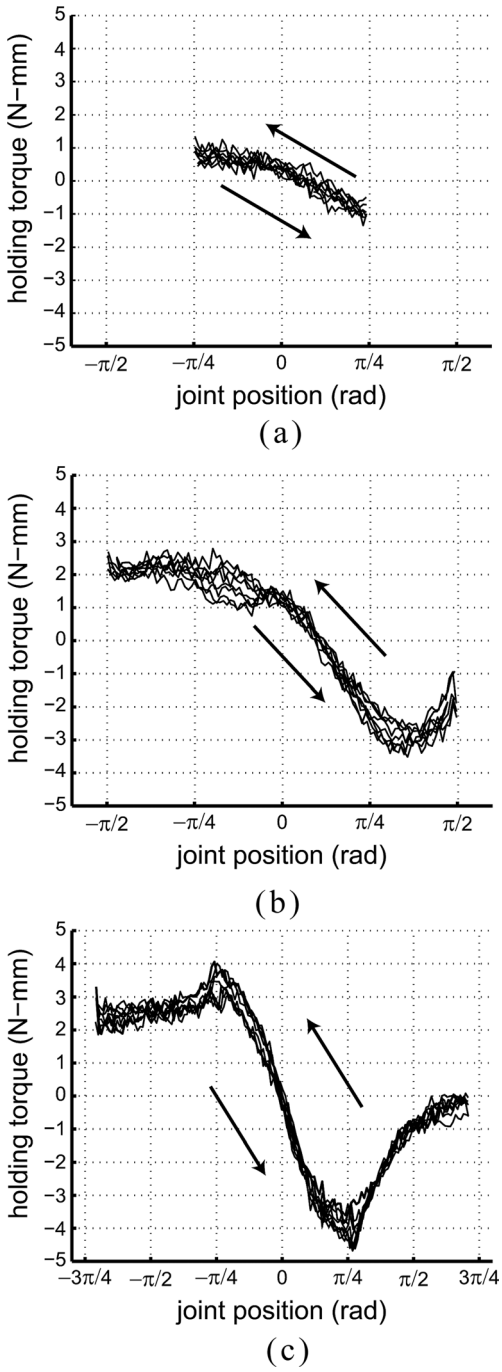


**Fig. 12 Holding torque versus joint position for hinge joints folded from 0.051 mm thick polyester film, with joint ranges $R = \pi/2, R = \pi$, and $R = 3\pi/2$. (*a*) $R = \pi/2$, (*b*) $R = \pi$, and (*c*) $R = 3\pi/2$.**

Figures 15 and 16 show the resulting curves for three of the joints folded from 0.051 mm and 0.127 mm thick polyester film, respectively. Active folds in a prismatic joint have fold angles that range from 0 to $\pi$, similar to the hinge joint with a range of motion of $\pi$ radians, so it is expected that the curves exhibit hysteresis. The figures also show the model proposed in Sec. 3 fitted to the data using a least squares fit over the stiffness and equilibrium positions for each row. For simplicity, we assumed that the stiffness values $k$ are constant and the same for each row of units. The shape of the experimental values matches well with the fitted curves. In general, the stiffness value was the same between forward and backward motion, while the equilibrium positions changed, which is consistent with our findings for the hinge joint.

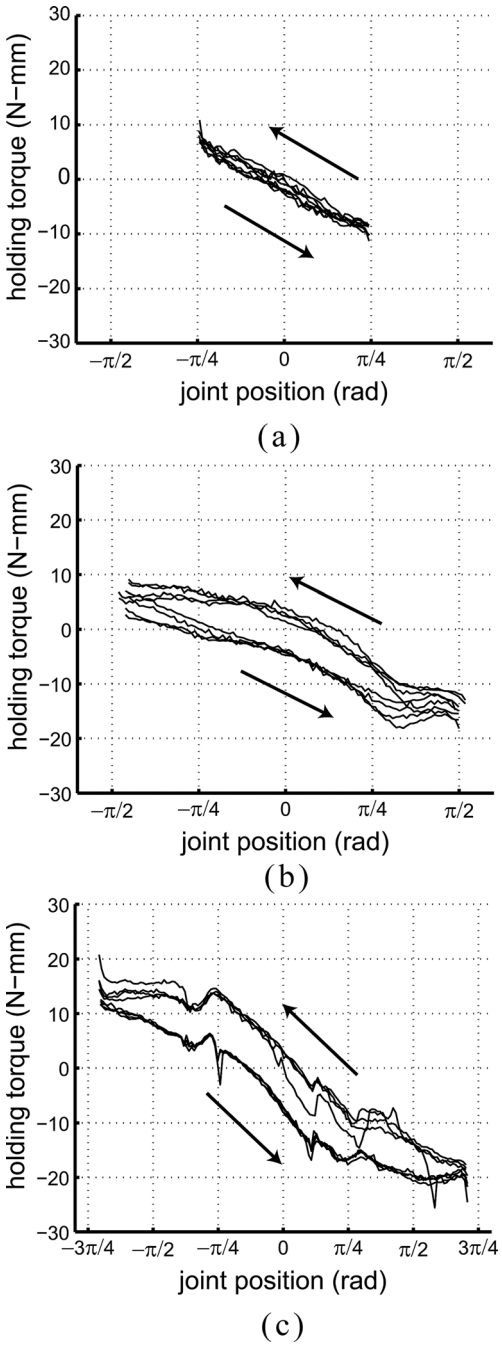


**Fig. 13 Holding torque versus joint position for hinge joints folded from 0.127 mm thick polyester film, with joint ranges $R = \pi/2, R = \pi$, and $R = 3\pi/2$. (*a*) $R = \pi/2$, (*b*) $R = \pi$, and (*c*) $R = 3\pi/2$.**

We suspect most of the approximation error can be attributed to nonlinearities in the spring constant. Large spikes in force such as those near 30 mm in Fig. 15(*b*) and near −60 mm in Fig. 16(*c*) occurred when the tabs that we added to facilitate folding snagged on other parts of the joint.

Table 1 shows the average stiffness values $k$ for each of the fitted curves. Stiffnesses for the thinner material are lower than for the thicker material by a factor of 13.1 in the mean. This is close to the theoretical factor of $(0.127\,\text{mm}/0.051\,\text{mm})^3 = 15.4$ derived from Eq. (6). Finally, the stiffness of a row increases with $N_c$. This is unsurprising since as $N_c$ increases, the number of active folds that contribute to the overall force also increases.

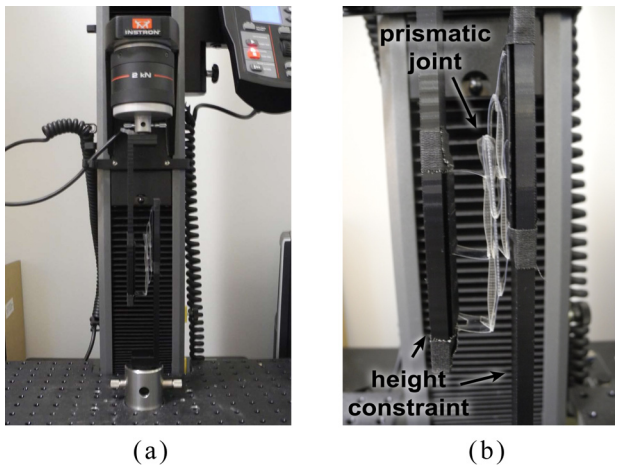


**Fig. 14 Experimental setup used to measure holding force of prismatic joints. (*a*) Experimental setup and (*b*) close-up of joint.**

*4.1.3 Pivot Joint.* We generated and folded three six-sided pivot joints ($r_o = 44$ mm) with 2, 4, and 6 layers, and we measured the holding torque for the joints using the setup shown in Fig. 17. The height of the joint was maintained at $\ell_s = 2r_o \sin(\pi/6) = 44$ mm throughout the tests. The joint was rotated clockwise at one step every 50 ms to the positive joint limit, then counterclockwise to the negative joint limit, for a total of four repetitions.

Plots of the results for each joint tested are shown in Figs. 18 and 19. Again, we fitted our model to the resulting data using a least squares fit over the stiffness and the equilibrium positions for each layer. We assumed the stiffness was the same for all layers and constant over the entire run. The model accurately captures the behavior of a pivot joint with two layers. As for $N_\ell = 4$ and $N_\ell = 6$, the model is able to capture the general topology and structure of the model, such as its periodicity. We believe the local errors are due to nonlinearities in the spring constant and to deformation of the faces during motion, which was not included in the model. This is supported by how the pivot joint appears to exhibit different behavior depending on the direction of rotation. As discussed in Sec. 2.4, the pivot joint cannot move rigidly, and so we have added cuts to the fold pattern, which more easily accommodate stretch when rotating clockwise than counterclockwise (refer Fig. 10(*b*)). For small deviations, the pseudo-rigid-body model we employed should be able to account for some elongation of faces [23]. Our results indicate that a deeper understanding of the joint requires more detailed models.

## 5 Composition of Folded Structures

Our system enables folded structures to be composed to produce more complex designs. In addition to generating joints, users can input custom patterns for folded structures as a vector drawing. They can then specify the edges or faces on individual folded structures that they wish to connect, and the system will combine the fold patterns of both into a single-sheet pattern for the composed structure [26]. The system provides views of both the flat fold pattern and its folded state in 3D so that users can visually verify that the composition is correct. We have tested this system for various joints, joint combinations, and linkage mechanisms.

**5.1 Joints With Higher Degrees of Freedom.** More complex joints with higher degrees of freedom can be created using our basic joints. In some cases, extra degrees of freedom come for free. For example, the designs for the prismatic and pivot joints each allow vertical translation in addition to the intended motion

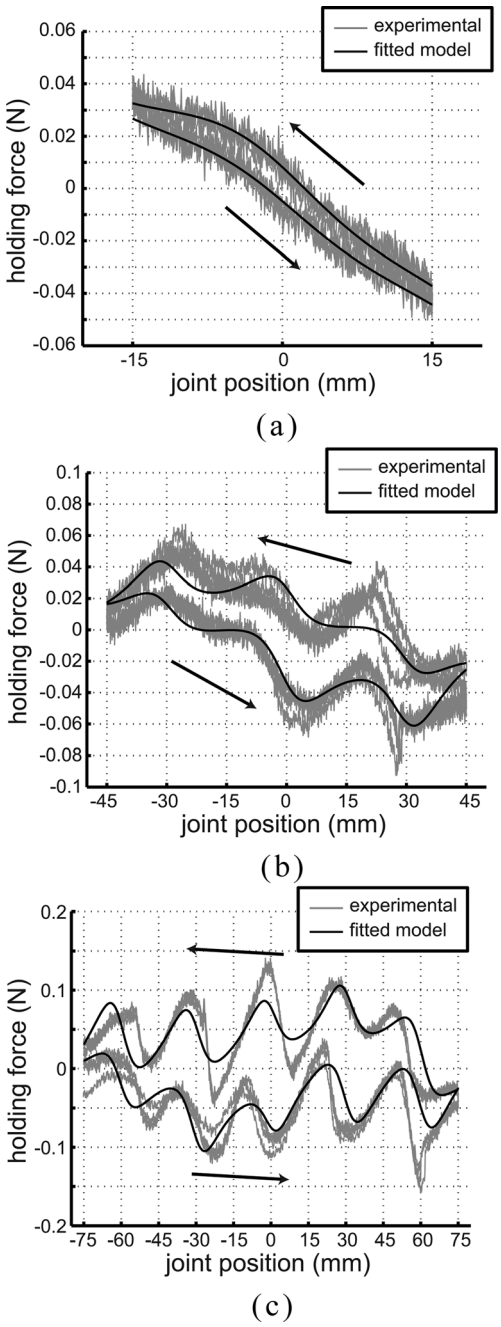


**Fig. 15 Holding force versus joint position for prismatic joints folded from 0.051 mm thick polyester film, overlaid with curves fitted from the model. (*a*) $N_c = 1$, $N_\ell = 2$, (*b*) $N_c = 2$, $N_\ell = 4$, and (*c*) $N_c = 4$, $N_\ell = 6$.**

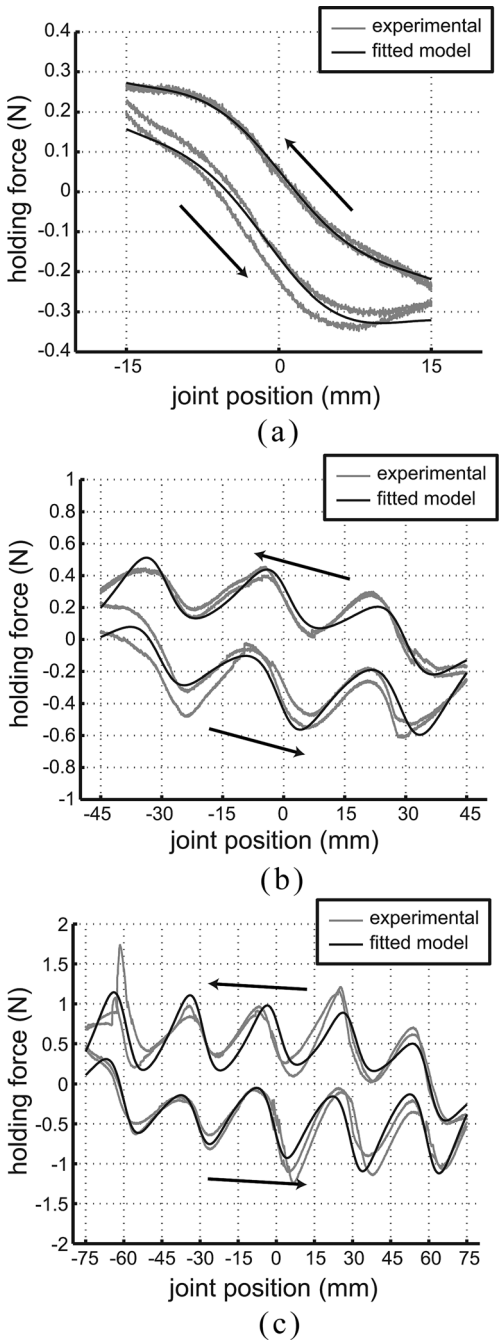


**Fig. 16 Holding force versus joint position for prismatic joints folded from 0.127 mm thick polyester film, overlaid with curves fitted from the model. (*a*) $N_c = 1$, $N_\ell = 2$, (*b*) $N_c = 2$, $N_\ell = 4$, and (*c*) $N_c = 4$, $N_\ell = 6$.**

when the height of the joint is not constrained. Thus, we can produce a cylindrical joint simply by removing the distance constraint between the outer faces of the pivot joint. When joints with higher degrees of freedom are created in this way, the joint limits for one degree of freedom will often depend on the position along the others. In other cases, joints can be combined. For example, a universal joint is two hinge joints with orthogonal axes of rotation connected in series. A spherical joint is a pivot joint combined with a hinge. Since our designs are parameterized, basic joints can be adjusted for simpler joining (e.g., by having the same base) without restricting the joint limits.

We tested joint composition by generating a spherical joint, shown in Fig. 20. The composed six-sided joint consists of a pivot joint with a $(10/3)\pi$ radian range of motion attached to a six-sided hinge joint with a $\pi$ radian range of motion. The fold patterns for the individual subcomponents are readily visible in the combined fold pattern for the entire joint. Since the axes of rotation of the pivot and hinge joints intersect at the center of the hinge joint, the resulting joint approximates well the behavior of a spherical joint, despite the pivot and hinge joint being two separate entities.

**5.2 Mechanisms.** Rigid bodies can be combined with our joints to produce entire foldable linkages. For example, we used our system to compose a four-bar linkage (Fig. 21). This linkage consists of four rectangular prisms, drawn manually, connected in

**Table 1 Fitted fold stiffness values *k* for prismatic joints made from two thicknesses of polyester film**

| | 0.051 mm thick film | | | 0.127 mm thick film | | |
|---|---|---|---|---|---|---|
| | $N_c = 1$ | $N_c = 2$ | $N_c = 4$ | $N_c = 1$ | $N_c = 2$ | $N_c = 4$ |
| $N_\ell = 2$ | 0.008 | 0.011 | 0.020 | 0.13 | 0.15 | 0.21 |
| $N_\ell = 4$ | 0.013 | 0.018 | 0.022 | 0.20 | 0.34 | 0.38 |
| $N_\ell = 6$ | 0.023 | 0.038 | 0.050 | 0.24 | 0.36 | 0.71 |
| $N_\ell = 8$ | 0.017 | 0.044 | 0.041 | 0.22 | 0.33 | 0.46 |

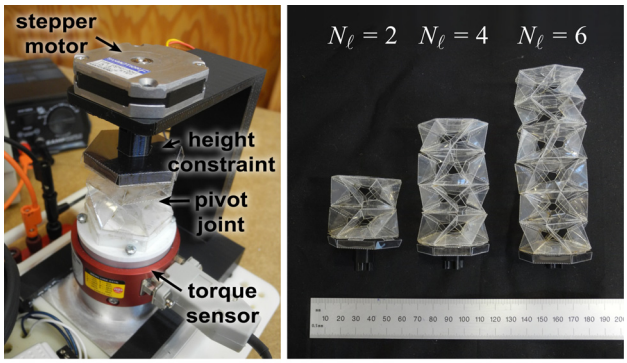


**Fig. 17 Experimental setup used to measure holding torque of the pivot joints. (*a*) Experimental setup and (*b*) tested pivot joints.**

a cycle using four pivot joints. A tubular structure similar to that in Figs. 10(*b*) and 20 was used to constrain the height of the pivot joints. We also manually designed a motor mount in order to actuate one joint and the linkage. Frames of the resulting motion are shown in Fig. 21(*b*). Since the joint angles are limited, the joint positions must be initialized carefully when folding to allow movement for the entire linkage.

In a second test, we composed two prismatic joints, two hinge joints, and a rectangular body to form a rowboat, shown in Fig. 22. The prismatic joints lie inside the rectangular body (Fig. 22(*c*)) and attach along the left and right edges. The top of the rectangular body forms the height constraint for the prismatic joint and enforces purely horizontal motion. On the other base of each prismatic joint is a paddle. Paddles are hinge joints with a $\pi/2$ radian range of motion mounted at a $\pi/4$ angle relative to the body of the boat to produce asymmetric joint limits. Thus, the paddles can lie horizontally over the water or can extend vertically down into the water to provide thrust.

## 6 Foldable Robots

Print-and-fold manufacturing enables using a single uniform process to fabricate entire robots. Actuation, sensing, and computation can be simultaneously incorporated into a robot during the fabrication process by printing circuitry and mounting components directly onto the fold pattern before folding. All of our joints provide natural placement for actuators and circuitry to be integrated into the folded structure, obviating the need for a postfolding stage of attaching circuit boards, actuators, and additional wires. In this section, we demonstrate joints and mechanisms with incorporated electronics.

We used the following procedure to fabricate all of our electromechanical devices. Circuit traces were printed on copper tape using a solid-ink printer. The tape was then affixed to a sheet of 0.127 mm thick polyester film, and the circuit etched out using a ferric chloride solution. The fold pattern was cut out and fold lines perforated on the reverse side of the polyester film using a laser cutter. Actuators, sensors, and other circuit components were soldered directly onto the circuit traces by hand. Finally, the device was folded into shape.

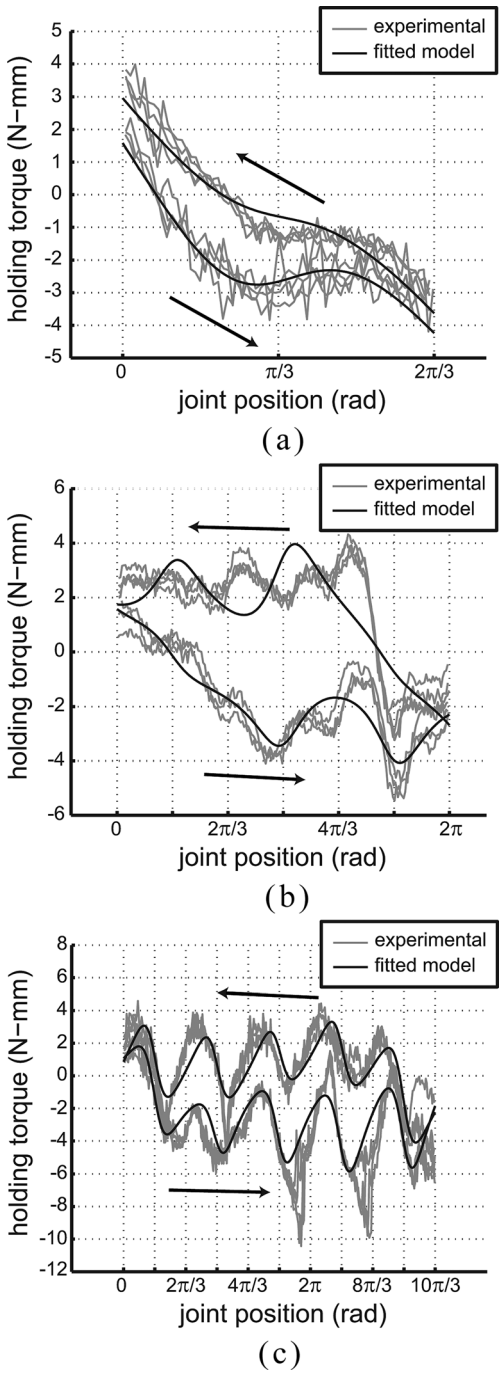


**Fig. 18 Holding torque versus joint position for pivot joints folded from 0.051 mm thick polyester film, overlaid with curves fitted from the model. (*a*) $N_\ell = 2$, (*b*) $N_\ell = 4$, and (*c*) $N_\ell = 6$.**

**6.1 Hinge Joint.** We used the design for a four-sided $\pi$ radian hinge joint and added a motor and potentiometer, as well as the control circuitry of a standard servo, to produce a hinge joint with position control. We placed the motor at the center of the hinge joint, with the output shaft aligned with the axis of rotation and

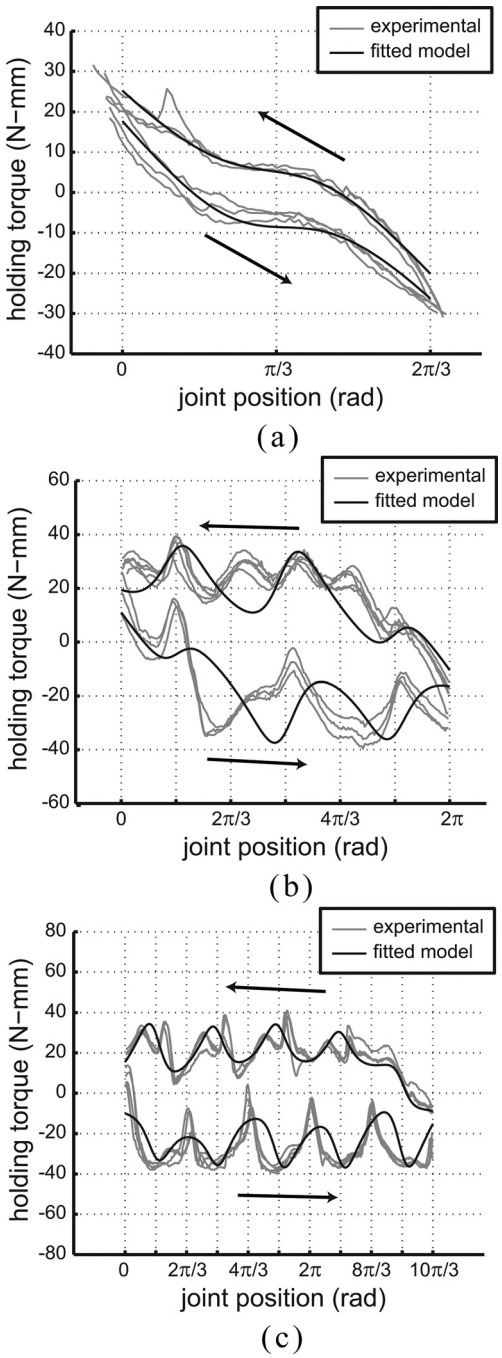


**Fig. 19 Holding torque versus joint position for pivot joints folded from 0.127 mm thick polyester film, overlaid with curves fitted from the model. (*a*) $N_\ell = 2$, (*b*) $N_\ell = 4$, and (*c*) $N_\ell = 6$.**

directly connected to the input of the potentiometer. We manually designed a motor mount (also used in the four bar linkage in Fig. 21) to keep the motor in place. The control circuit was designed by hand and line the faces of the bottom half of the joint.

The final hinge is pictured in Fig. 23. Despite the motor and potentiometer leads being on opposite sides of the hinge joint, both components were able to be soldered directly into the circuit without additional wires. We sent a pulse width modulation signal to the microcontroller on the joint to control its angle. The joint was able to achieve the entire $\pi$ radian range for which it was designed. This joint demonstrates the feasibility of integrating sensors and actuators directly with our fold patterns to produce foldable robots.

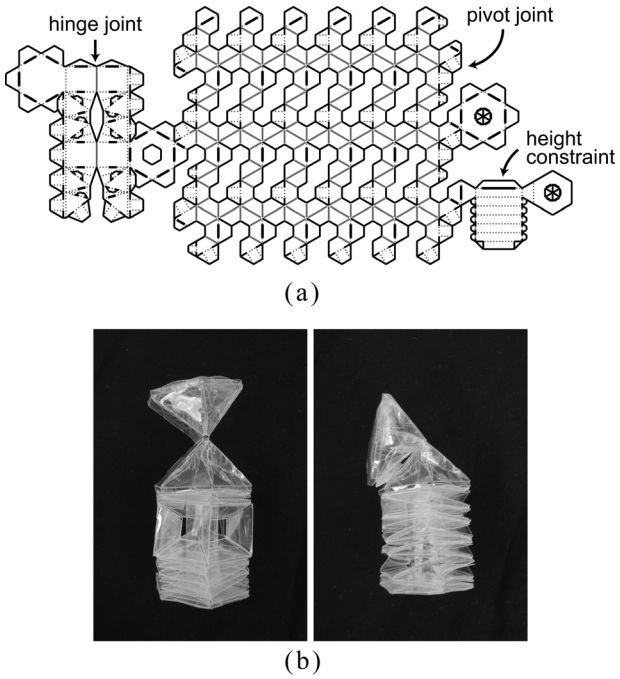


**Fig. 20 Spherical joint composed from six-sided pivot and hinge joints. (*a*) Composed fold pattern (with tabs and slots) and (*b*) folded joint in two positions.**

**6.2 Crane.** When our system composes folded structures, the original fold patterns are preserved in their entirety. This feature enables us to reuse our circuit layouts. Starting from the actuated hinge from Sec. 6.1, we added square bars and three more four-sided $\pi$ radian hinge joints to produce a four-bar linkage, and we composed the entire linkage with a six-sided $2\pi$ radian pivot mount to produce a machine with kinematics similar to those of a manufacturing crane (Fig. 24). To the hinge circuitry, we simply added the additional control circuitry for a DC motor mounted at the center of the pivot joint. Finally, we added circuitry for serial communication via a Digi XBee radio module so that the robot could be controlled wirelessly. Commands were sent from a laptop, which controlled the direction of rotation of the pivot mount and the position of the hinge joint.

During testing, the hinge joint on the robot performed exactly as the original hinge joint did, although its range of motion was restricted due to the additional hinges and links attached to it. The pivot joint was able to achieve its full $2\pi$ radian range of motion.

**6.3 Camera Mount.** As a final test, we composed a mount for a smartphone with the spherical joint shown in Fig. 20, yielding a camera mount with pan-tilt capabilities (Fig. 25), and we actuated both degrees of freedom independently using off-the-shelf servos. Again circuitry was designed by hand and etched directly onto the robot body, except for the servos, which were plugged into headers in the circuit. A laptop sent commands to tilt forward or backward or to pan left or right via serial communication through a Digi XBee radio module.

The spherical joint in the camera mount was designed for $(3/2)\pi$ radians of pan and $(2/3)\pi$ radians of tilt. During testing, the camera was able to achieve the full $(3/2)\pi$ radians of pan. However, since small servos are typically not designed to sustain large loads such as the weight of a smartphone, tilt had to be limited to $\pm(\pi/4)$ radians when a smartphone was in place. Since over half of the weight of the device lay above the hinge joint (camera mount: 91 g, smartphone: 116 g), the mount would bend or even topple when large tilt angles were attempted.

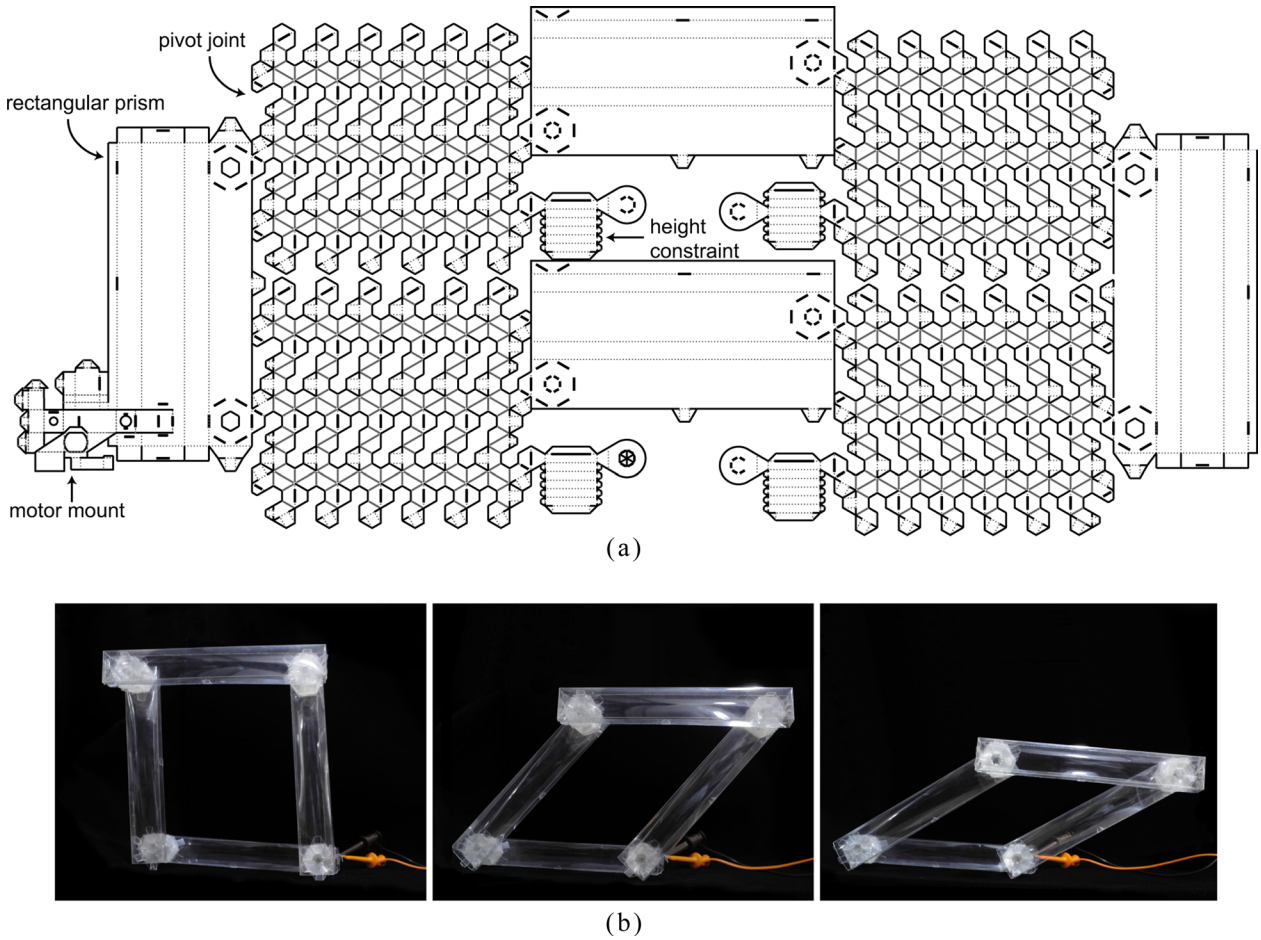


**Fig. 21 Foldable four-bar linkage. (*a*) Composed fold pattern and (*b*) movement of four-bar.**

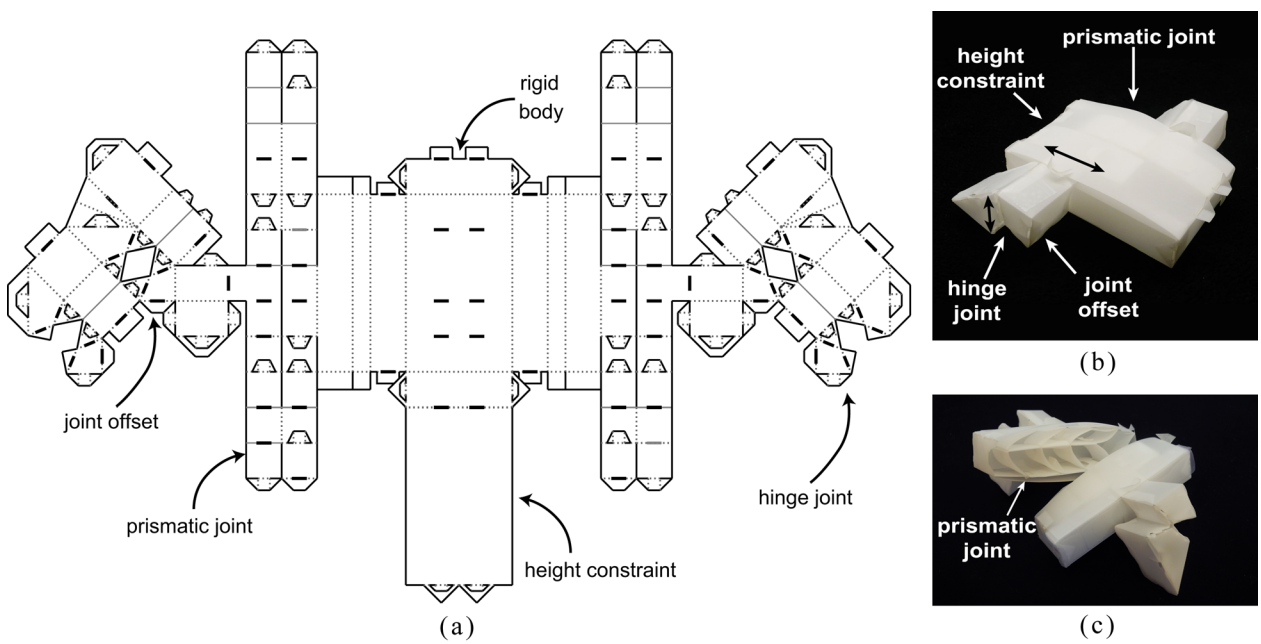


**Fig. 22 Foldable rowboat. (*a*) Composed fold pattern, (*b*) folded rowboat, and (*c*) section cut showing interior.**

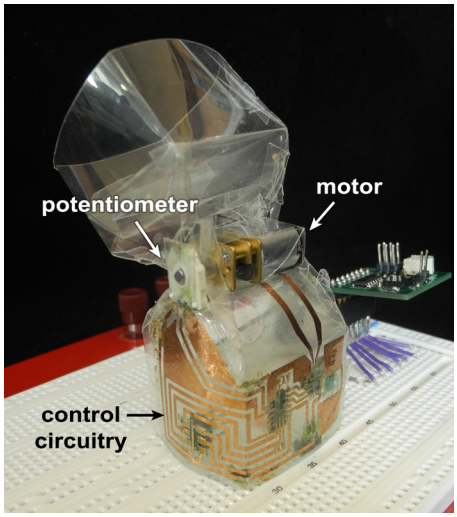


**Fig. 23 Hinge joint with integrated electronics**

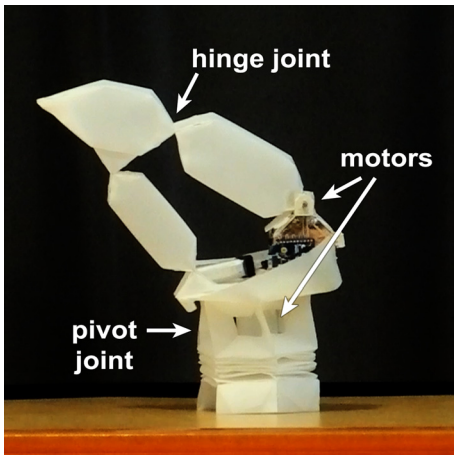


**Fig. 24 Actuated four-bar linkage atop actuated pivot mount**

## 7 Discussion and Future Work

Our work demonstrates the feasibility of print-and-fold manufacturing for robots, a manufacturing paradigm that enables an entire robot to be created in one uniform process. We have presented designs for foldable joints, and we have shown not only that joints can be folded but also that their fold patterns can be combined into fold patterns for entire robot bodies. Our fold patterns are parameterized to deliver the range of motion needed by the robot application, and they can be composed to achieve the full range of joint types. The joints are controllable using electronic components that can be added during the printing process.

Further work must be done to achieve robots that can be fabricated using planar rapid printing processes. First, although linkages are an important component of many robot designs, other common mechanisms should be investigated to see if folding can truly achieve any robot. Second, when folding robots from thin materials, strength, stiffness, and an actual ability to transfer and withstand high forces and torques becomes a concern. The camera mount, although stable for small angles, was top heavy when a smartphone was inserted, and it would become unstable when large displacements were attempted. We have shown here that simple spring-based models may not be sufficient, since a fold's behavior is dependent on the movements it has previously experienced. Multilayered structures may also require more complex

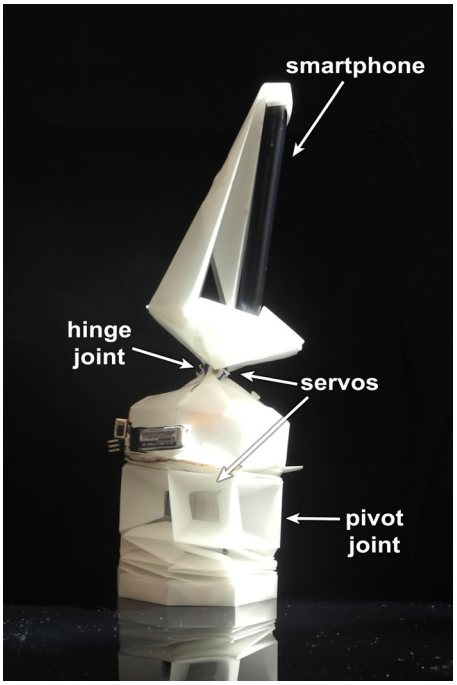


**Fig. 25 Smartphone mount attached to actuated spherical joint to allow pan and tilt**

models. Future work includes better characterization of the mechanical properties of folded structures and the dynamics of folded joints, so that print-and-fold robots can achieve the functionality, not just the movement, which they need.

## Acknowledgment

This work was funded in part by NSF Grant Nos. 1240383 and 1138967, and by the Department of Defense through the National Defense Science & Engineering Graduate Fellowship Program. We thank Vijay Kumar for helpful comments and suggestions, and Thomas Bertossi for his assistance with force and torque measurements.

## References

[1] Hoover, A. M., Steltz, E., and Fearing, R. S., 2008, "RoACH: An Autonomous 2.4 g Crawling Hexapod Robot," IEEE/RSJ International Conference on Intelligent Robots and Systems (IROS 2008), Nice, France, Sept. 22–26, pp. 26–33.

[2] Onal, C., Wood, R., and Rus, D., 2013, "An Origami-Inspired Approach to Worm Robots," IEEE/ASME Trans. Mechatronics, **18**(2), pp. 430–438.

[3] Soltero, D. E., Julian, B. J., Onal, C. D., and Rus, D., 2013, "A Lightweight Modular 12-DOF Print-and-Fold Hexapod," IEEE/RSJ International Conference on Intelligent Robots and Systems (IROS), Tokyo, Japan, Nov. 3–7, pp. 1465–1471.

[4] Mehta, A., and Rus, D., 2014, "An End-to-End System for Designing Mechanical Structures for Print-and-Fold Robots," IEEE International Conference on Robotics and Automation (ICRA), Hong Kong, May 31–June 7, pp. 1460–1465.

[5] Niiyama, R., Rus, D., and Kim, S., 2014, "Pouch Motors: Printable/Inflatable Soft Actuators for Robotics," IEEE International Conference on Robotics and Automation (ICRA), Hong Kong, May 31–June 7, pp. 6332–6337.

[6] Mehta, A. M., DelPreto, J., Shaya, B., and Rus, D., 2014, "Cogeneration of Mechanical, Electrical, and Software Designs for Printable Robots From Structural Specifications," IEEE/RSJ International Conference on Intelligent Robots and Systems (IROS 2014), Chicago, IL, Sept. 14–18, pp. 2892–2897.

[7] Demaine, E., and O'Rourke, J., 2008, *Geometric Folding Algorithms: Linkages, Origami, Polyhedra*, Cambridge University Press, New York.

[8] Lee, D., Kim, J., Kim, S., Koh, J., and Cho, K., 2013, "The Deformable Wheel Robot Using Magic-Ball Origami Structure," ASME Paper No. DETC2013–13016.

[9] Gao, W., Ramani, K., Cipra, R. J., and Siegmund, T., 2013, "Kinetogami: A Reconfigurable, Combinatorial, and Printable Sheet Folding," ASME J. Mech. Des., **135**(11), p. 111009.

[10] Whitney, J., Sreetharan, P., Ma, K., and Wood, R., 2011, "Pop-Up Book MEMS," J. Micromech. Microeng., **21**(11), p. 115021.

[11] Abel, Z., Demaine, E. D., Demaine, M. L., Eisenstat, S., Lubiw, A., Schulz, A., Souvaine, D. L., Viglietta, G., and Winslow, A., 2013, "Algorithms for Designing Pop-Up Cards," 30th International Symposium on Theoretical Aspects of Computer Science (STACS'13), Kiel, Germany, Feb. 27–Mar. 2, pp. 269–280.
[12] Tachi, T., and Miura, K., 2012, "Rigid-Foldable Cylinders and Cells," J. Int. Assoc. Shell Spat. Struct. (IASS), **53**(4), pp. 217–226.
[13] Mitani, J., and Suzuki, H., 2004, "Computer Aided Design for Origamic Architecture Models With Polygonal Representation," Computer Graphics International (CGI '04), Crete, Greece, June 19, pp. 93–99.
[14] Winder, B. G., Magleby, S. P., and Howell, L. L., 2009, "Kinematic Representations of Pop-Up Paper Mechanisms," ASME J. Mech. Rob., **1**(2), p. 021009.
[15] Bowen, L. A., Grames, C. L., Magleby, S. P., Howell, L. L., and Lang, R. J., 2013, "A Classification of Action Origami as Systems of Spherical Mechanisms," ASME J. Mech. Des., **135**(11), p. 111008.
[16] Lee, H., and Choi, Y., 2010, "Stackable 4-Bar Mechanisms and Their Robotic Applications," IEEE/RSJ International Conference on Intelligent Robots and Systems (IROS), Taipai, Taiwan, Oct. 18–22, pp. 2792–2797.
[17] Zhu, L., Xu, W., Snyder, J., Liu, Y., Wang, G., and Guo, B., 2012, "Motion-Guided Mechanical Toy Modeling," ACM Trans. Graphics, **31**(6), p. 127.
[18] Coros, S., Thomaszewski, B., Noris, G., Sueda, S., Forberg, M., Sumner, R. W., Matusik, W., and Bickel, B., 2013, "Computational Design of Mechanical Characters," ACM Trans. Graphics, **32**(4), p. 83.
[19] Thomaszewski, B., Coros, S., Gauge, D., Megaro, V., Grinspun, E., and Gross, M., 2014, "Computational Design of Linkage-Based Characters," ACM Trans. Graphics, **33**(4), p. 64.
[20] Mitra, N. J., Yang, Y.-L., Yan, D.-M., Li, W., and Agrawala, M., 2010, "Illustrating How Mechanical Assemblies Work," ACM Trans. Graphics, **29**(4), p. 58.
[21] Sung, C., and Rus, D., 2014, "Foldable Joints for Foldable Robots," International Symposium on Experimental Robotics (ISER 2014), Marrakech/Essaouira, Morocco, June 15–18.
[22] Howell, L., Midha, A., and Norton, T., 1996, "Evaluation of Equivalent Spring Stiffness for Use in a Pseudo-Rigid-Body Model of Large-Deflection Compliant Mechanisms," ASME J. Mech. Des., **118**(1), pp. 126–131.
[23] Howell, L. L., 2001, *Compliant Mechanisms*, Wiley, New York.
[24] Qiu, C., Aminzadeh, V., and Dai, J. S., 2013, "Kinematic Analysis and Stiffness Validation of Origami Cartons," ASME J. Mech. Des., **135**(11), p. 111004.
[25] Dai, J. S., and Cannella, F., 2008, "Stiffness Characteristics of Carton Folds for Packaging," ASME J. Mech. Des., **130**(2), p. 022305.
[26] Sung, C., Demaine, E. D., Demaine, M. L., and Rus, D., 2013, "Edge-Compositions of 3D Surfaces," ASME J. Mech. Des., **135**(11), p. 111001.